PROCEEDINGS, 43rd Workshop on Geothermal Reservoir Engineering
Stanford University, Stanford, California, February 12-14, 2018
SGP-TR-213

Overview and Preliminary Results from the PoroTomo project at Brady Hot Springs, Nevada: Poroelastic Tomography by Adjoint Inverse Modeling of Data from Seismology, Geodesy, and Hydrology

Kurt L. FEIGL

Department of Geoscience, University of Wisconsin-Madison, 1215 West Dayton Street, Madison, WI, 53706 United States

feigl@wisc.edu

The PoroTomo Team, including Elena C. REINISCH(1), Jeremy R. PATTERSON (1), Samir JREIJ(7), Lesley PARKER(1), Avinash NAYAK(1), Xiangfang ZENG(1,9), Michael A. CARDIFF(1), Neal E. LORD (1), Dante FRATTA(1), Clifford H. THURBER(1), Herbert F. WANG(1), Michelle ROBERTSON(2), Thomas COLEMAN(3), Douglas E. MILLER(3), Paul SPIELMAN(4), John AKERLEY(4), Corné KREEMER(5), Christina MORENCY(6), Eric MATZEL(6), Whitney TRAINOR-GUITTON(7), Nicholas C. DAVATZES(8)

(1) University of Wisconsin-Madison, Department of Geoscience, Madison, WI, United States;
(2) Lawrence Berkeley National Laboratory, Berkeley, CA, United States;
(3) Silixa, Houston, TX, United States;
(4) Ormat Technologies Inc., Reno, NV, United States;
(5) University of Nevada Reno, NV, United States;
(6) Lawrence Livermore National Laboratory, Livermore, CA, United States;
(7) Colorado School of Mines, Golden, CO, United States;
(8) Temple University, Philadelphia, PA, United States;
(9) State Key Laboratory of Geodesy and Earth's Dynamics, Institute of Geodesy and Geophysics, Chinese Academy of Sciences
http://geoscience.wisc.edu/feigl/porotomo/

Keywords: EGS, DAS, DTS, GPS, INSAR

Abstract

In the geothermal field at Brady Hot Springs, Nevada, subsidence occurs over an elliptical area that is ~4 km by ~1.5 km. Highly permeable conduits along faults appear to channel fluids from shallow aquifers to the deep geothermal reservoir tapped by the production wells. Results from inverse modeling suggest that the deformation is a result of volumetric contraction in units with depth less than 600 m [*Ali et al.*, 2016]. Characterizing such structures in terms of their rock-mechanical properties is essential to successful operations of Enhanced Geothermal Systems (EGS). The goal of the PoroTomo project is to assess an integrated technology for characterizing and monitoring changes in the rock-mechanical properties of an EGS reservoir in three dimensions with a spatial resolution better than 50 meters. In March 2016, we deployed the integrated technology in a 1500-by-500-by-400-meter volume at Brady Hot Springs. The data set includes: active seismic sources, fiber-optic cables for Distributed Acoustic Sensing (DAS) and Distributed Temperature Sensing (DTS) arranged vertically in a borehole to ~400 m depth and horizontally in a trench 8700 m in length and 0.5 m in depth, 244 seismometers on the surface, three pressure sensors in observation wells, continuous geodetic measurements at three GPS stations, and seven InSAR acquisitions. The deployment consisted of four distinct time intervals ("stages"). Between each measurement interval, the hydrological conditions were intentionally manipulated by modifying the rates of pumping in the injection and production wells. To account for the mechanical behavior of both the rock and the fluids, we are developing numerical models for the 3-dimensional distribution of the material properties. In this paper, we provide a snapshot of work in progress, including the highlights listed in the Conclusions below. The work presented herein has been funded in part by the Office of Energy Efficiency and Renewable Energy (EERE), U.S. Department of Energy, under Award Number DE-EE0006760.

1. INTRODUCTION

In the geothermal field at Brady Hot Springs, Nevada, subsidence occurs at a rate of the order of a centimeter per year over an elliptical area that is ~4 km by ~1.5 km, as measured by satellite interferometric synthetic aperture radar (InSAR) and mapped in Figure 1. Results from inverse modeling suggest that the deformation is a result of volumetric contraction in units with depth less than 600 m. [*Ali et al.*, 2016]. Highly permeable conduits along faults appear to channel fluids from shallow aquifers to the deep geothermal reservoir tapped by the production wells, as sketched in Figure 2.

The objective of the PoroTomo project is to assess an integrated technology for characterizing and monitoring changes in an enhanced geothermal system (EGS) reservoir in three dimensions with a spatial resolution better than 50 meters. The targeted characteristics include: saturation, porosity, Young's modulus, Poisson's ratio, and density, all of which are "critically important" to a viable EGS reservoir (DOE GTO, 2014). Estimating these parameters and their uncertainties will contribute to the overarching goal of characterizing the reservoir in terms of its effective permeability and/or fracture transmissivity. The technology performance metric for the project is resolution in meters of a feature in the modeled 3-D distribution of a rock mechanical property (e.g., Poisson's ratio), as determined by the dimension of a visible checkerboard pattern at 200 m depth in a test using simulated data. Resolution is controlled by: the number of parameters to be estimated in the inverse problem, the number of measurements, and the distribution of the sensors. For

seismic data, the wavelength and distribution of the sources also play crucial roles. During Phase I of the project, we accomplished a proof of concept. We have validated the computational analysis techniques by adapting and applying them to existing data sets [*Ali et al.*, 2016; *Lancelle*, 2016; *Lord et al.*, 2016; *Zeng et al.*, 2017a].

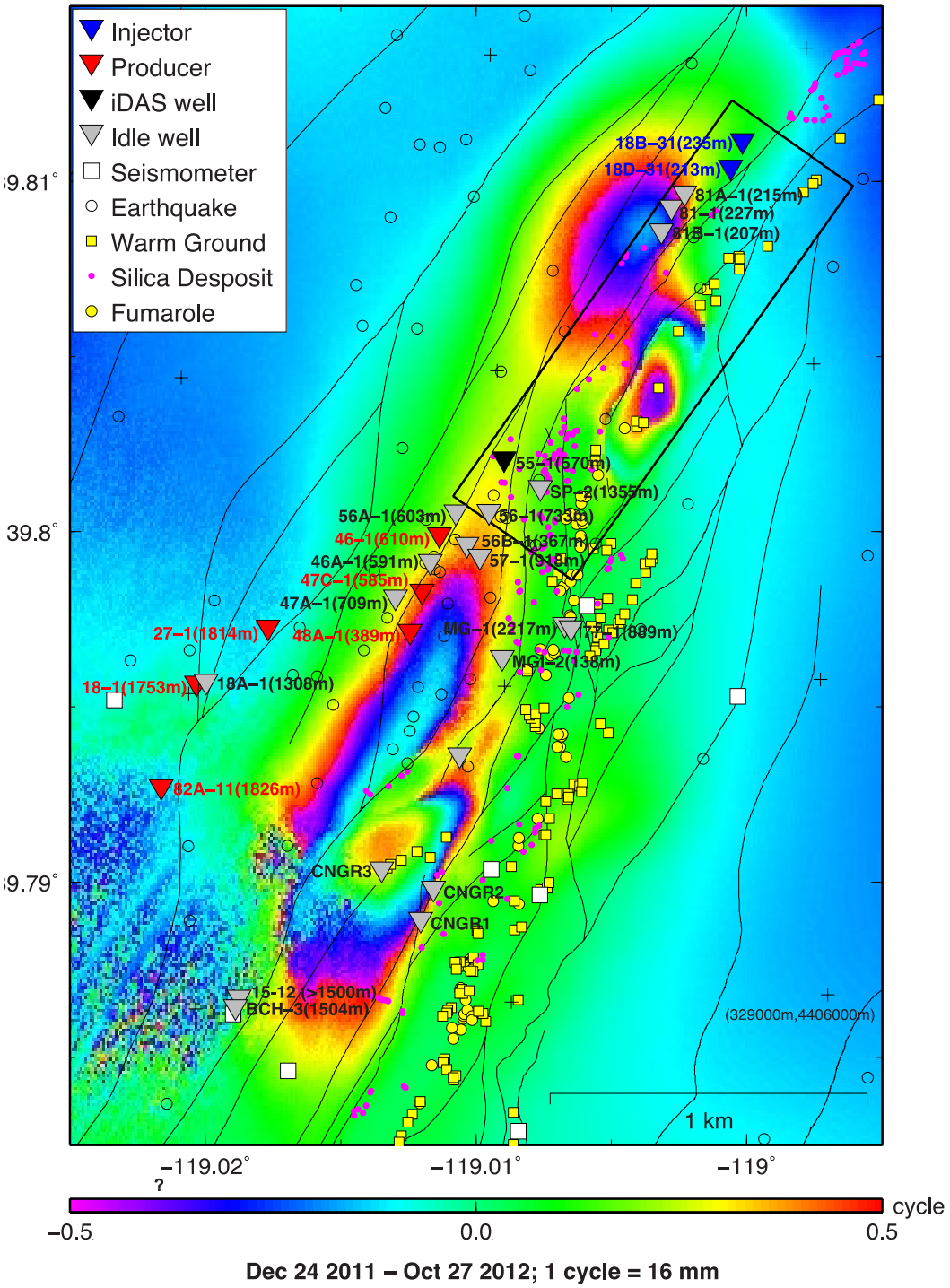

Figure 1. Map showing location of the Brady Hot Springs geothermal field, with faults (thin black lines, [*Faulds et al.*, 2010], surface hydrothermal activity, including fumaroles (yellow circles), warm ground (yellow squares), and silica deposits (magenta circles) from precise field mapping [*Coolbaugh et al.*, 2004]. Injection wells are shown by blue triangles and producing wells are shown by red triangles. Fiducial crosses indicate 1000-meter grid in easting and northing of the Universal Transverse Mercator (UTM) projection (Zone 11). The SAR interferogram in the background shows the change in wrapped phase over the 308-day interval from December 24, 2011 to October 27, 2012. One colored fringe corresponds to one cycle of phase change, or 16 mm of range change. The dotted and dashed grey line delimits the broad subsiding zone. The black rectangle delimits the study area of the PoroTomo project.

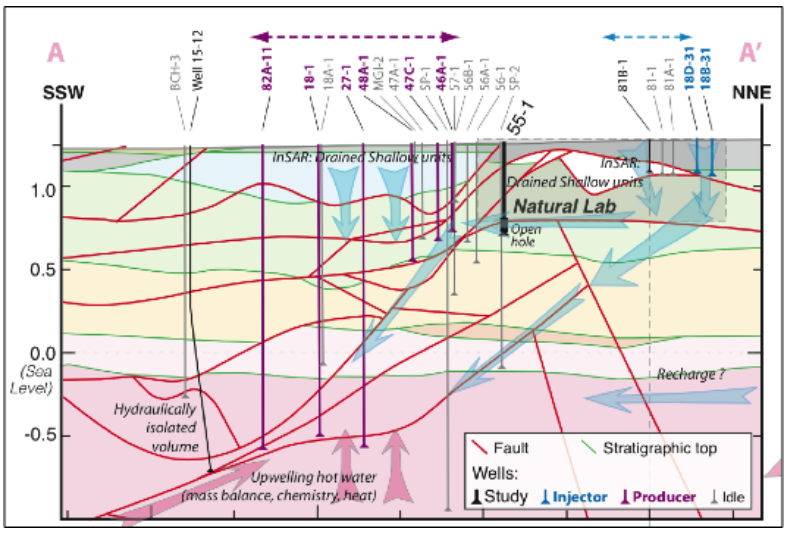

Figure 2. Sketch of vertical cross section, showing the key idea that highly permeable conduits along faults channel fluids from shallow aquifers to the deep geothermal reservoir tapped by the production wells. Vertical cross section based on geologic model of Jolie, Moeck and Faulds and geologic mapping by Faulds [*Faulds et al.*, 2004; *Faulds et al.*, 2006; *Faulds et al.*, 2011; *Shevenell et al.*, 2012; *Jolie et al.*, 2015]. Elevation in km. V:H = 1:1.

2. DEPLOYMENT AT BRADY HOT SPRINGS DURING MARCH 2016

In Phase II of the project, we are working to demonstrate a prototype of an integrated technology at the EGS field at Brady Hot Springs, Nevada. The study area is a shallow volume with length ~1500 m, width ~500 m, and depth ~400 m, as delimited by the black rectangle in Figure 1. In March 2016, we deployed the proposed technology during four distinct time intervals, as illustrated in Figure 3. Between each measurement interval, the hydrological conditions were intentionally manipulated by modifying the rates of pumping in the injection and production wells. By comparing the four sets of results, we expect to quantify any temporal changes in the characteristics of the study volume.

Day of experiment	before	1	2	3	4	5	6	7	8	9	10	11	12	13	14	15	after
Calendar Date		2016-03-11	2016-03-12	2016-03-13	2016-03-14	2016-03-15	2016-03-16	2016-03-17	2016-03-18	2016-03-19	2016-03-20	2016-03-21	2016-03-22	2016-03-23	2016-03-24	2016-03-25	
day of week		Friday	Saturday	Sunday	Monday	Tuesday	Wednesday	Thursday	Friday	Saturday	Sunday	Monday	Tuesday	Wednesday	Thursday	Friday	
Stage 1: Normal operations																	
Stage 2: shutdown- stop injection and production																	
Stage 3: divert all injection to infield wells																	
Stage 4: Resume normal operations																	
Expected water level		normal			rising / dropping	higher / lower			rising / ? or ?	highest			normal				
Acquire SAR Image																	
Operate Active Seismic Source																	
Operate seismometers																	
Operate DAS and DTS																	
Operate Pressure Sensors																	

Figure 3. Schedule of operations during deployment at Brady Hot Springs in March 2016, showing pumping operations (upper rows), expected level of groundwater (arrows), and data streams (lower rows).

We are analyzing measurements from three data sets: (1) seismic waveforms recorded by seismometers and distributed acoustic sensors (DAS); (2) the deformation of the Earth's surface recorded by satellite geodesy, including the Global Positioning System (GPS) and Interferometric Synthetic Aperture Radar (InSAR); and (3) time series of hydraulic pressure, flow, and temperature measured in wells for production, injection, or observation. The details of the data sets are described elsewhere [*Feigl and PoroTomo_Team*, 2017].

Below, we update that report. All of the data became available to the public on October 1st, 2017 at ftp://roftp.ssec.wisc.edu/porotomo. Metadata describing each of these data sets are available at the Geothermal Data Repository (GDR): https://gdr.openei.org/search?q=porotomo&submit=Search.

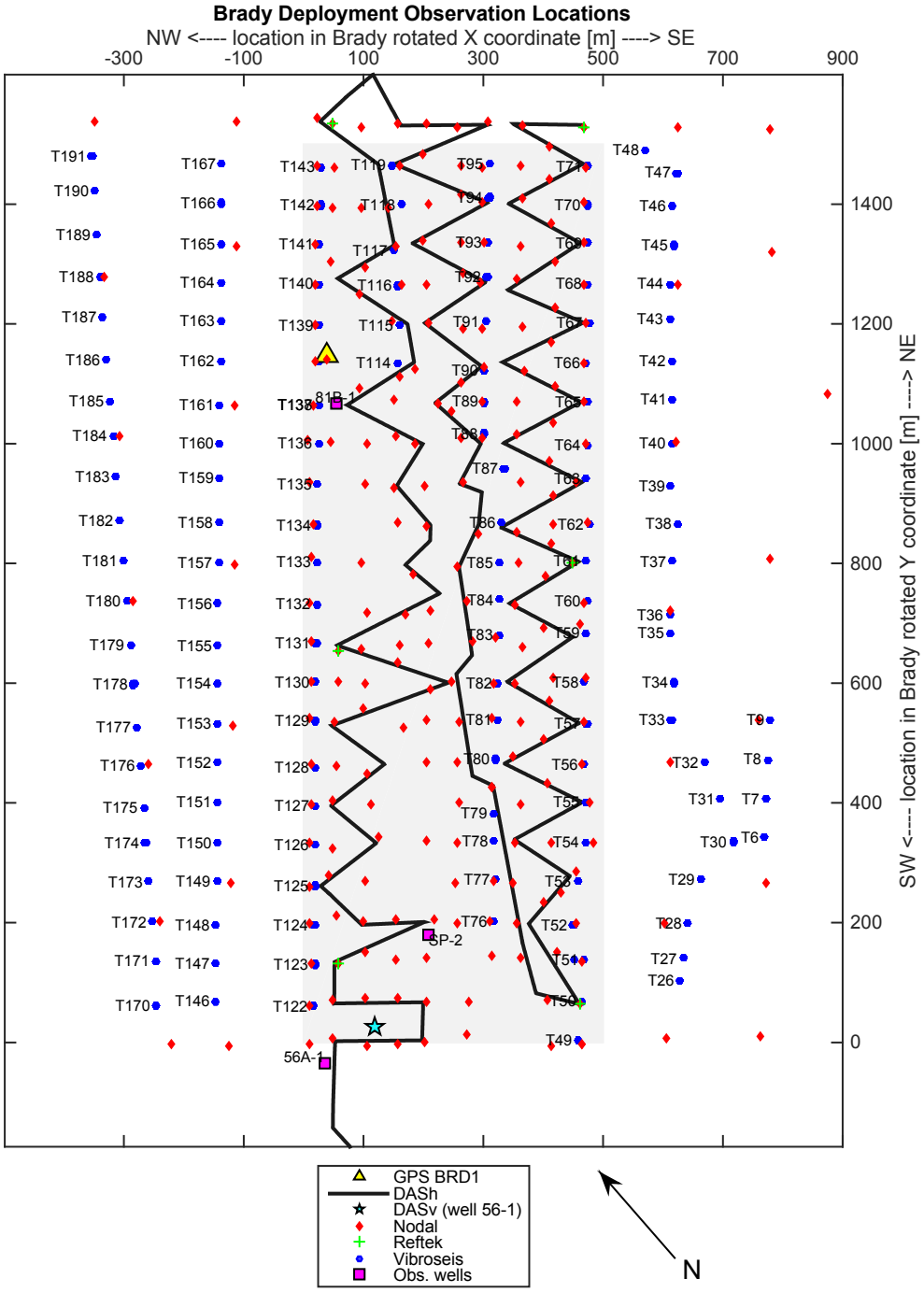

Figure 4. Map of study area, showing volume targeted for tomography (gray shading), vibroseis points (blue hexagons, labeled Tnnn), Nodal seismometers (red diamonds), Reftek seismometers (green crosses), fiber-optic cable (black line) for distributed acoustic sensing (DAS) and distributed temperature sensing (DTS), GPS station BRD1 (yellow triangle). A separate fiber optical cable for DAS and DTS was deployed vertically in the borehole of Well 56-1 (blue star). The Y-axis of the rotated coordinate system is approximately parallel to the northeast-striking fault system.

In the following sections, we describe the networks of instrumentation deployed in March 2016. The 3-dimensional position of each instrument was surveyed with centimeter-level accuracy using Real Time Kinematic (RTK) GPS. In addition, we present some preliminary results from each data set.

3. HYDROLOGY

In March 2016, we monitored pressure and temperature at several wells. The details of the instrumentation as well as the metadata describing the monitoring boreholes are available on the GDR [*Lim*, 2016]. Briefly, the monitoring locations consisted of a shallow well near where water is re-injected (81B-1), a deep well near the main area of production (56A-1), and a well located halfway between these two points (SP-2) [*Lim*, 2017]. In addition, pumping data, including flow rates, temperature and pressure are available for the production and injection wells that were in operation during the deployment [*Akerley*, 2016].

To analyze the hydrological data sets, we are estimating reservoir properties from the time series of pressure data. Specifically, we seek to estimate hydraulic conductivity K and specific storage S_s. Multiple conceptual models are being tested to determine the necessary level of model complexity required to fit the collected data. The numerical groundwater flow model is developed using MODFLOW [*Harbaugh*, 2005]. The model domain is 7 km x 13 km x 6 km (x, y, z). The model is oversized to prevent boundary effects on the numerical solutions, with model boundaries determined using simulated dipole pumping tests and determining the distance at which drawdown is less than 10 cm. The model takes an equivalent porous medium approach and assumes that at a large enough scale, the reservoir can be modeled as a non-fractured porous medium with effective hydraulic properties.

To determine these effective hydraulic properties, parameter estimation is conducted using PEST [*Doherty*, 2001], a common parameter estimation software package that interfaces nicely with MODFLOW. The parameters to be estimated are K_x, K_y, K_z, and S_s. The reservoir is assumed to be isotropic; therefore, K_x = K_y. K_z is tied to K_x so that each parameter will change in the same direction by the same value. This reduces the number of adjustable parameters per zone from 4 to 2, reducing the model run times and the overall inversion time. There is no regularization imposed on the inversion. The current conceptual model that provides the best fit to the observed data consists of 3 hydraulic zones. These zones are grouped based on identified lithologic units [*Jolie et al.*, 2012; *Siler et al.*, 2016] that are assumed to have similar hydraulic properties. Zone 1 (purple) consists of Tertiary sedimentary deposits, Zone 2 (yellow) consists of grouped Tertiary lacustrine sedimentary deposits, and Zone 3 (green) consists of grouped volcanic and metamorphic basement rock. Pressure data collected during plant shutdown (Stage 2) are used for the parameter estimation. Five points, out of more than 6000 data points, are chosen for fitting with PEST. The best-fitting estimated parameters and associated misfit are shown in Figure 5. More details have been described by Patterson et al. [2017a].

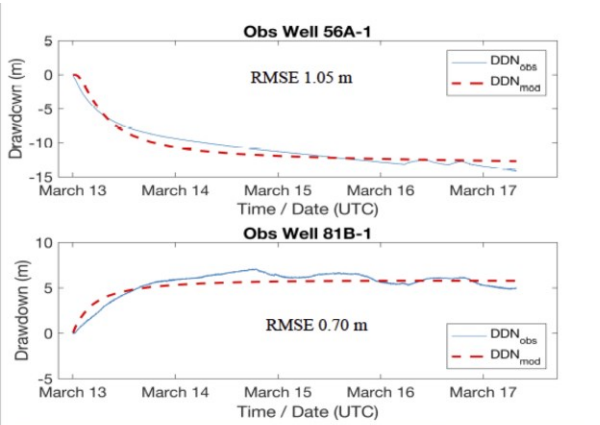

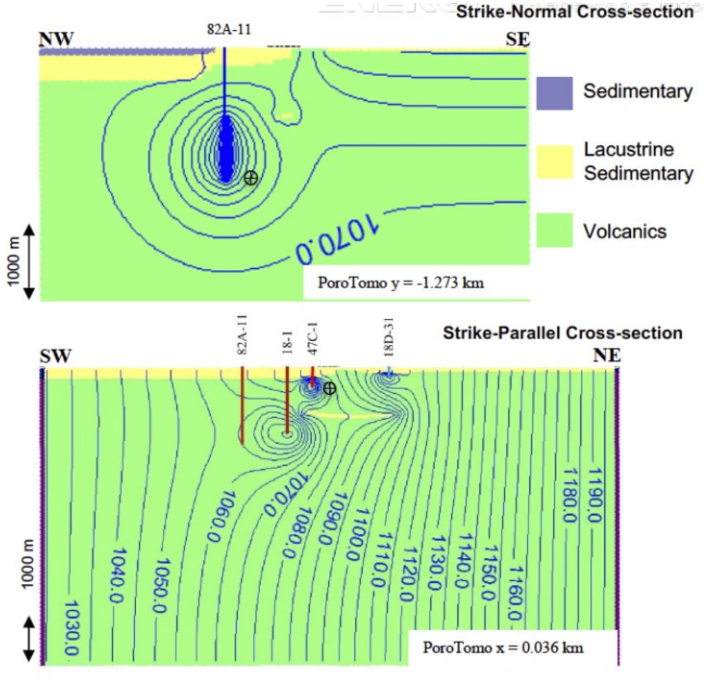

Rock type	Hydraulic conductivity K_{eff} (m/s)	Specific storage S_s (m^{-1})
Sedimentary	2.3×10^{-4}	2.2×10^{-8}
Lacustrine Sed.	6.3×10^{-4}	1.3×10^{-6}
Volcanics	1.2×10^{-8}	1.1×10^{-6}

Figure 5. Results of hydrogeological analysis, showing: At upper left, pressure changes (as meters of water) as observed (solid blue curve) and simulated (dashed red curve) in two different wells. At right: two vertical slices of the model immediately prior to shutdown showing effect of extraction and injection on initial pressures with contours of hydraulic head in meters. Strike-normal fiducial point is (Xp= 0, Zp= -0.598). Strike-parallel fiducial point at (Yp= 0, Zp= 0.649). At lower left, table showing estimated values of hydraulic conductivity and specific storage for each of the three zones in the model.

4. GEODESY

As described previously, the geothermal field at Brady Hot Springs, Nevada has subsided over the past decade [*Ali et al.*, 2016; *Reinisch et al.*, 2017; *Reinisch et al.*, in prep]. Between 2004 and 2014, the rate of downward vertical displacement was of the order of 10 mm/year, as measured by geodetic techniques: Interferometric synthetic aperture radar (InSAR) and Global Positioning System (GPS). Here we consider the deformation field mapped by InSAR data spanning 2016-July-22 to 2017-August-22 (Figure 6). The observed deformation field forms an approximately elliptical bowl that is 4 km long and aligned with the trace of the normal fault system that strikes NNE, as shown in Figure 6.

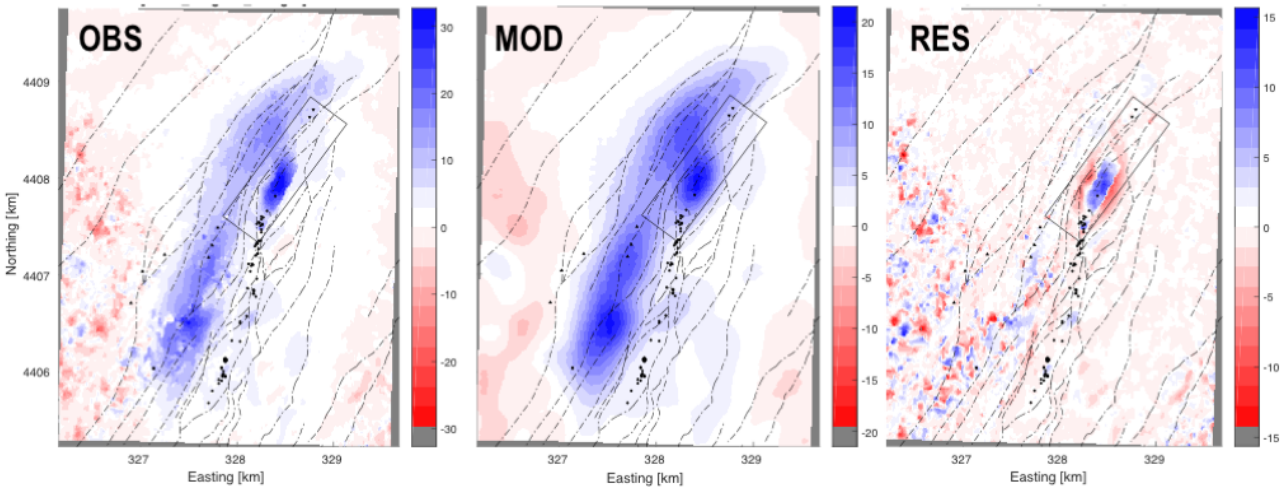

Figure 6. InSAR data spanning 2016-July-22 to 2017-August-22, showing deformation in unwrapped range change rate [mm/yr]: as observed by the TerraSAR-X satellite mission (left), as modeled under the hypothesis of thermal contraction (center), and the residual field as calculated from the observed field minus the modeled field (right). [*Reinisch et al.*, 2017; *Reinisch et al.*, in prep].

We also GPS measurements of displacement [*Reinisch et al.*, 2017; *Reinisch et al.*, in prep]. Three GPS stations operated continuously during the deployment. Station BRD1 was installed on the head of completed Well 18-1 on 10 March 2016. It is located inside the study area, near the center of the area undergoing rapid subsidence, as mapped by InSAR. GPS stations BRAD and BRDY are located outside the study area at distances of approximately 5 and 3 km from BRD1, respectively. All three GPS stations are part of the MAGNET network operated by the Geodesy Lab at the University of Nevada in Reno. The procedures for analyzing the data have been described previously [*Blewitt et al.*, 2013].

To validate the InSAR measurements of deformation, we compare them to the GPS measurements. We convert the GPS measurement of the displacement at BRD1 with respect to BRDY to range change by taking the negative scalar product with a unit pointing vector from the pixel on the ground toward the satellite. We use the location of BRDY to characterize the deformation in the far field. From the interferogram in Figure 6, we select a set of pixels the southeast corner of the study area, where little deformation is observed. Similarly, we select another set of pixels in the subsiding bowl near BRD1. The difference between the InSAR range change values averaged over these two sets gives the component of relative displacement along the line of sight from the satellite to the ground. The results listed Table 1 indicate that the difference between the two types of measurements is insignificantly different from zero with 95 percent confidence [*Reinisch et al.*, 2017; *Reinisch et al.*, in prep].

	$\overline{\Delta\rho} \pm \sigma$ [mm]
GPS	13.45 ± 2.88
InSAR	9.87 ± 3.29
DIFF	3.58 ± 6.17

Table 1. Comparison of range change values between points located at stations BRD1 and BRDY as measured by GPS and InSAR on 2016-July-22 to 2017-August-22 [*Reinisch et al.*, 2017; *Reinisch et al.*, in prep].

To simulate the deformation field, we use a formal inversion to estimate the parameters in a model of contracting dislocations buried in a half space with uniform elastic properties [*Reinisch et al.*, in prep]. Using Bayesian inference, we test two hypotheses to explain the deformation field: (1) declining pore-fluid pressure and (2) thermal contraction. As shown in Figure 7, the model that best fits the InSAR data spanning the time interval between 22 July 2016 and 22 August 2017 estimates the rate of volume change in the modeled

reservoir to be (–2.9 ± 0.1) × 10^4 cubic meters per year, the total volume of the cooling part of the modeled reservoir to be 1.1 × 10^8 cubic meters, and the rate of thermal work in the cooling part of the reservoir to be −56 to −75 megawatt.

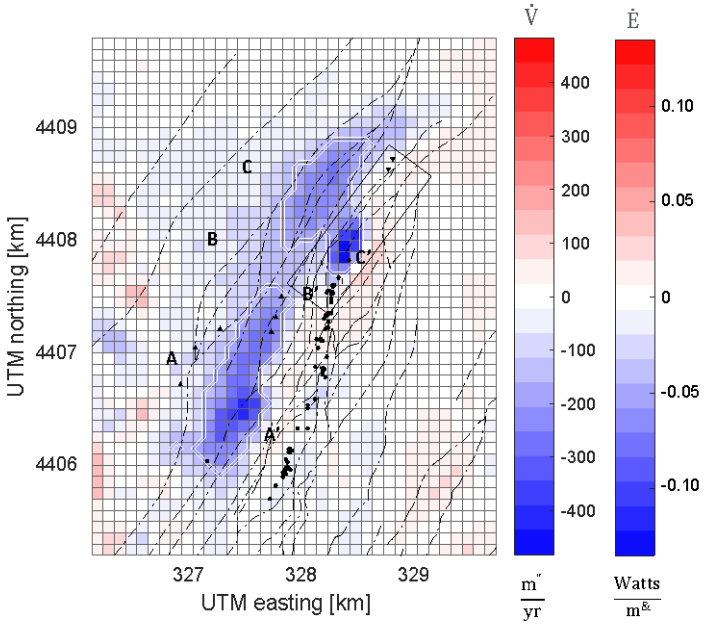

Figure 7. Results of inverse modeling of InSAR data under the hypothesis of thermal contraction, showing the values of estimated parameters of thermal strain rate per voxel (from inversion with a temperature-defined model) color-coded and interpreted in terms of volume change rate and thermal energy change rate. Black filled circles are fumarole locations. Dashed lines are faults. Inverted triangles are injection well locations. Upright triangles are production well locations. Area where PoroTomo focused on during deployment is shown with rectangular outline. Letters correspond to cross sections done from 3D analysis (not shown or discussed here).

5. SEISMOLOGY

Instrumentation

A crew from the University of Texas-Austin operated a vibrating source named T-REX. The vibration protocol included three sweeps for each of P, transverse S, and longitudinal S at each of approximately 200 locations during each of the four stages of the 15-day field experiment. Using associated coder/decoder telemetry units, the vibroseis truck operated in synchronization with the DAS array and the conventional seismometers. For each of the three modes, the vibroseis source made three sweeps over 20 seconds. Each sweep increased in frequency from 5 Hz to 80 Hz.

The seismic instrumentation included 238 Zland 3-component sensors manufactured by FairfieldNodal. Each of these instruments (dubbed "Nodals") has a corner frequency of 5 Hz, a 24-bit digitizer with a dynamic range of 127 dB, and a timing accuracy of ±10 microseconds from a GPS receiver [*FairfieldNodal*, 2015]. Between March 11 and March 26, 2016, these instruments operated and recorded autonomously and continuously with sampling interval of 0.002 s (i.e. a sampling rate of 500 samples per second) for the entire two-week deployment without any human intervention. Arrays of *single-component*, 10-Hz Nodal instruments have been utilized for many scientific projects, including at Long Beach, CA [*Lin et al.*, 2013], but the PoroTomo experiment is one of the first academic uses of the newer *three-component* 5-Hz Nodal instruments.

The seismic network also included six 3-component seismic stations from the national instrumentation program named Portable Array Seismic Studies of the Continental Lithosphere (PASSCAL). Each station included an L28 model, 4.5-Hertz, 3-component geophone, Reftek RT130 seismograph, and a GPS timing clock.

We also used Distributed Acoustic Sensing (DAS) — the first such deployment in a geothermal field in North America. The "intelligent" Distributed Acoustic Sensing (iDAS^{TM}) system uses a continuous length of fiber-optic cable as an array of seismic sensors [e.g., *Parker et al.*, 2014]. This technology transmits pulses of light into the fiber and records the response from its Rayleigh backscatter. The resulting measurement is sensitive to the rate of transient strain along the axis of the cable. At Brady, the instrumentation included 8700 meters of DAS cable buried horizontally in a shallow trench and 400 meters of DAS cable hanging vertically in Well 56-1. The DAS data were recorded continuously, archived in 30-second files in SEG-Y format [*Barry et al.*, 1975]. More than 60 Terabytes of DAS data were collected over the four stages of the PoroTomo experiment in March 2016. To understand the DAS recordings, we review a few of their characteristics [*Bakku*, 2015; *Daley et al.*, 2015]. DAS measures the strain rate $\dot{\varepsilon}$ in the fiber by averaging its elongation over a segment of cable (called the "gauge length") during a temporal sampling interval. The elongation represents the phase shift of the backscattered light pulse. These data were written with dimensions of radians per millisecond in the SEG-Y files. In this DAS system, one radian of phase change corresponds to 116 nanometers of elongation. The wavelength of the laser light is 1550 nanometer. The temporal sampling interval was set to 1 millisecond and the spatial sampling length was set to 1 meter. The spatial resolution of the DAS strain rate measurement equals the gauge length of 10 m. Further comparisons of the ground motions recorded by the two arrays (DAS cable and Nodal seismometers) are underway [*Wang et al.*, 2016; *Wang et al.*, submitted 2017/10/03].

P-wave velocity from 3-D seismic tomography

We have performed 3-dimensional seismic tomography to estimate P-wave velocity [*Parker*, 2017; *Thurber et al.*, 2017]. The cross-correlation method was utilized to remove the sweep signal from the geophone and DAS records. The first P arrivals were automatically picked from the cross-correlation results using a combination of methods, and the travel times were used to invert for the 3D P-wave velocity structure. Models with horizontal node spacing of 50 m and 100 m were obtained, with vertical node spacing of 10 to 50 m. The travel time data were fit to about 30 ms, close to our estimated picking uncertainty. As seen in Figure 8, the boundaries between high and low velocity zones agree with previous surveys of local faults. Low velocity zones near the surface correspond to fumarole locations.

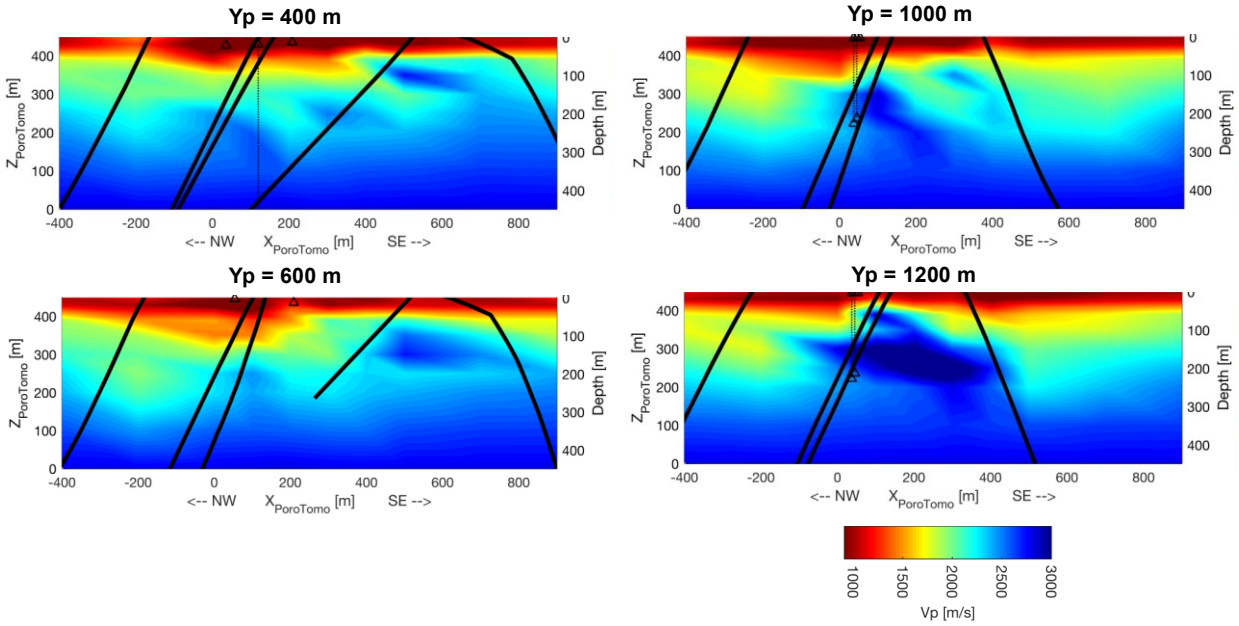

Figure 8. P-wave velocity estimated from body-wave tomography [*Thurber et al.*, 2017]. Each panel shows a vertical slice perpendicular to the NE-SW strike of the fault system. Black lines show faults tessellated from a geologic model [*Jolie et al.*, 2015] based on field observations .

To evaluate the performance metric of spatial resolution of the estimated P-wave velocity, we performed a checkerboard test [*Thurber et al.*, 2017]. The results appear in Figure 9. For the 100-meter checkerboard test, the velocity at 200 m depth was recovered within 1% of the true value for 69% of the natural lab area, and for the central part of the natural lab, recovery was within 0.1% on average. For the 50-meter checkerboard test, the velocity at 200 m depth was recovered within 1% of the true value for 32% of the natural lab area, and for the central part of the natural lab, recovery was within 0.2% on average.

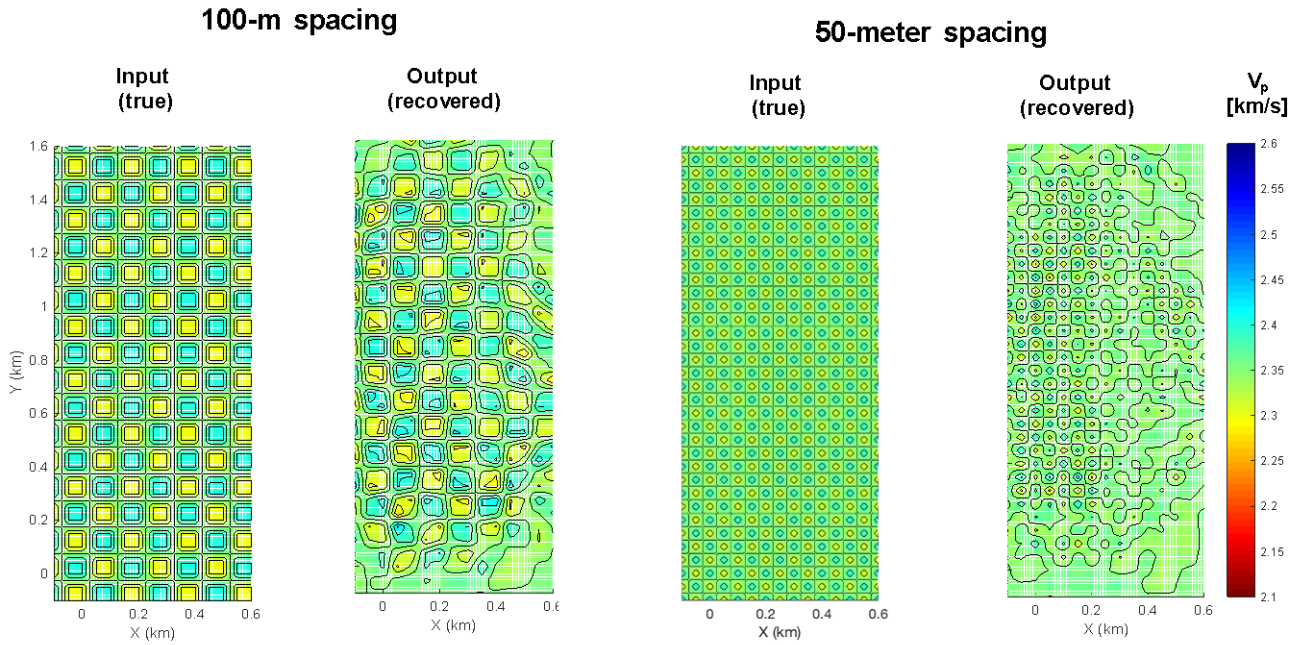

Figure 9. Results of a checkerboard test of resolution of P-wave velocity at 200 m depth, showing, from left to right, input (true) values with 100-meter spacing, output (recovered) values with 100-meter spacing, input (true) values with 50-meter spacing, and output (recovered) values with 50-meter spacing.

Sweep Interferometry

Sweep interferometry uses the energy from the vibroseis sweeps as sources of high frequency energy [*Matzel et al.*, 2017b]. The data recorded at one seismometer are correlated with the data recorded at another to obtain an estimate of the Green's function between the two. Figure 10 shows the values of several material properties in a horizontal slice at a depth of 225 m as inferred by this method. Further details are presented at this meeting [*Matzel et al.*, 2018].

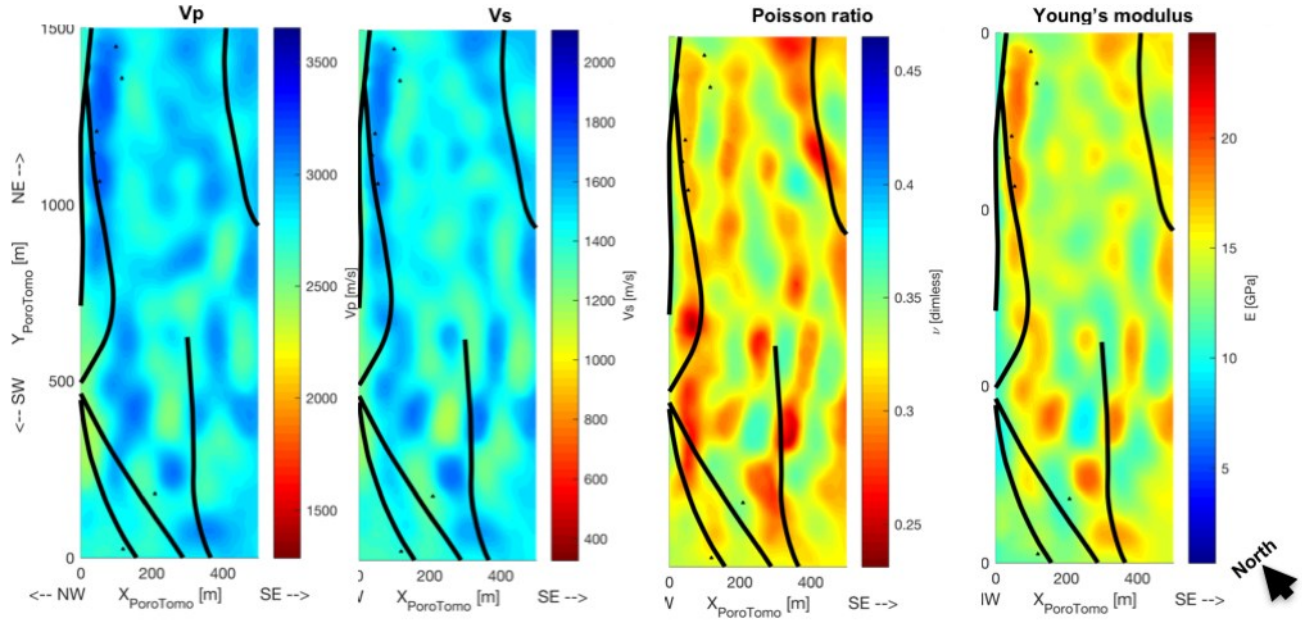

Figure 10. Material properties at a depth of 225 m below mean ground surface estimated using sweep interferometry: From left: P-wave velocity, S-wave velocity, Poisson's ratio, and Young's modulus (calculated using the density values from a gravimetric study [*Witter et al.*, 2016]). Black lines show faults tessellated from a geologic model [*Jolie et al.*, 2015] based on field observations .

MASW on NCFs from DAS data

Using the DAS data recorded continuously over hours, we have calculated Noise Correlation Functions [*Zeng et al.*, 2017b]. These functions are then inverted via Multichannel Analysis of Surface Waves (MASW) to estimate shear-wave velocity at shallow depth. The results appear in horizontal slices in Figure 11. The uppermost deposits are very heterogeneous and include diatomaceous earth, silt, sand, and hardened silica associated with the presence of fumaroles, as observed by field mapping [*Faulds and Garside*, 2003; *Coolbaugh et al.*, 2004; *Faulds et al.*, 2004; *Faulds et al.*, 2010].

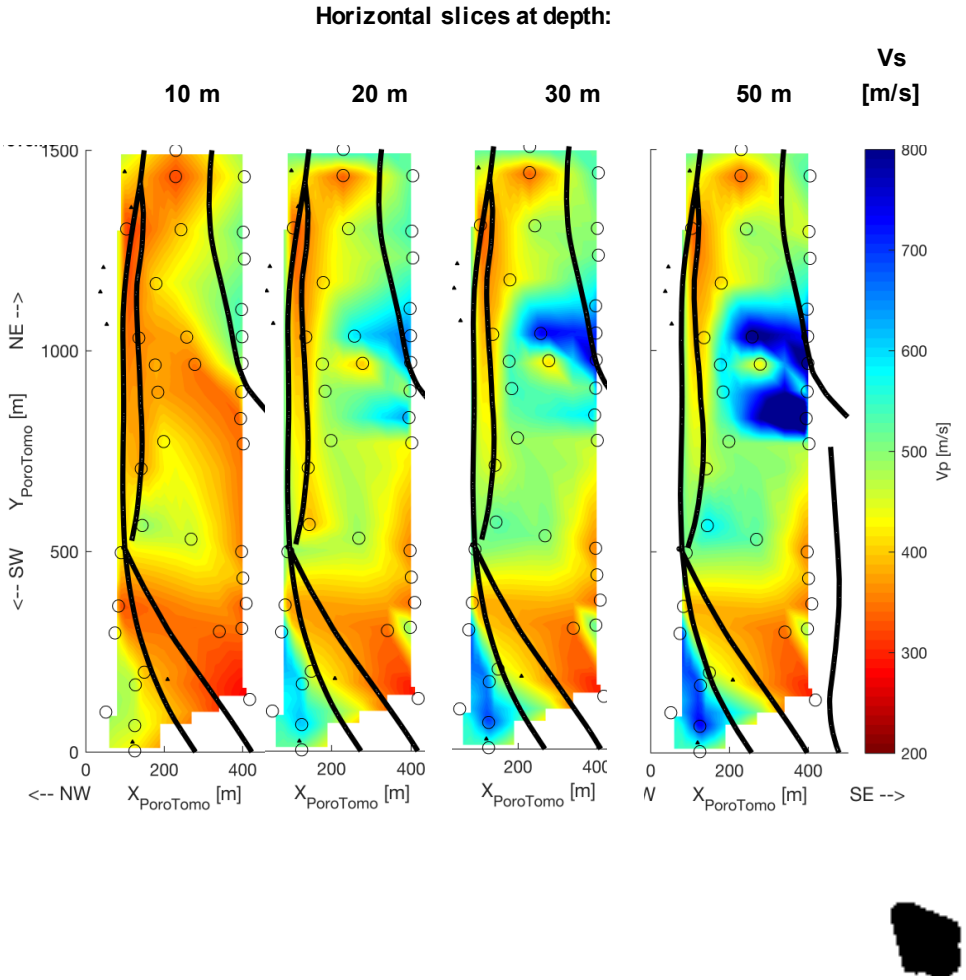

Figure 11. Shear-wave velocity estimated from Multichannel Analysis of Surface Waves (MASW) on Noise Correlation Functions (NCFs) derived from Distributed Acoustic Sensing (DAS) data. Horizontal slices at four different depths are shown.

DAS data recorded in a borehole

We consider the vibration response as a function of depth and time from sweeps at two different vibroseis stations recorded by the vertical DAS array in the borehole of Well 56-1. The raw DAS data were converted to fiber strain and correlated with the accelerometer response of the vibrating baseplate in the vibroseis truck. In particular, we compare the responses from two vibroseis stations with about 260 m offset distances but on opposite sides of the well. Both records show compressional arrivals, some of which may be reflections. The strong blue amplitudes indicate a down-going shear signal. An up-going shear signal converted from a down-going P wave at a boundary near 300-m depth is also apparent. The compressional signals match the modeled values more closely than do the shear-wave arrivals. These disagreements are likely caused by differences in the near-surface properties in the vicinity of the two source locations. More details are presented at this meeting [*Miller et al.*, 2018].

Distributed Temperature Sensing

The same fiber optic cables also performed distributed temperature sensing – DTS [e.g., *Coleman*, 2013]. At Brady, the DTS data have been analyzed and published [*Patterson et al.*, 2017b]. Further details are presented at this meeting [*Patterson et al.*, 2018].

CONCLUSIONS

Body-wave seismic tomography achieved the target resolution of 50 meters for P-wave velocity at 200 m depth for much of the natural lab using P-wave arrival times picked from the waveforms recorded by Fairfield Nodal seismometers and Distributed Acoustic Sensing (DAS) in fiber-optic cable [*Parker*, 2017; *Thurber et al.*, 2017].

Seismic sweep interferometry using data recorded by geophones during active source sweeps estimated a 3-D model of Vs, Vp, Q, and Poisson's ratio with a resolution of the order of ~100 m at a depth of 200 m [*Matzel et al.*, 2017a; *Matzel et al.*, 2017b; *Matzel et al.*, 2018].

Deploying DAS effectively quadrupled the number of seismic sensors, provided DTS capability simultaneously, and demonstrated the value of the technology for seismic characterization of a geothermal reservoir.

Shear-wave velocities estimated from surface wave dispersion curves based on Noise Correlation Functions (NCF) from DAS data showed horizontal variations with resolution ~100 m and vertical variations with resolution of ~10 m at depths less than 50 m.

Analysis of InSAR data spanning 2004-2017 using a dislocation model estimates the rate of volume change to be (29 ± 1) thousand cubic meters per year and the rate of thermal work in the cooling part of the reservoir to be −56 to −75 megawatt.

GPS data at 3 stations BRDY, BRAD and BRD1 from 2016 through 2017 have been collected, archived, distributed, and analyzed to yield time series of daily estimates of relative, 3-dimensional position [https://gdr.openei.org/submissions/999].

Structured parameter estimation on pump testing data estimates hydraulic conductivity and storage coefficient with a spatial resolution comparable to the 500-meter distance between sensors [*Patterson et al.*, 2017a].

The DTS data set has been analyzed to characterize heat flow within the reservoir during production and injection with a vertical resolution of the order of 0.1 meter [*Patterson et al.*, 2017b].

Data on pressure, temperature, production, and injection at Brady for the time interval 2004-2014 favor the hypothesis that injecting cooled water causes thermal contraction as the dominant process driving the deformation field observed by geodetic data [*Reinisch et al.*, in prep].

ACKNOWLEDGMENTS

We are extremely grateful to Fan-Chi Lin (University of Utah), Amanda Thomas (University of Oregon), and Marianne Karplus (University of Texas-El Paso) for contributing their Fairfield Nodal Zland 3-component sensors to our project. We thank all those who lent helping hands in the field (sorted in reverse alphabetical order by given name): Xuyang Liu, Xiangfang Zeng, Thomas Coleman, Tanner Whetstone, Stoyan Nikolov, Sin-Mei Wu, Scott Nelson, Robert Kent, Rob Skarbek, Paul Spielman, Neal Lord, Mike Cardiff, Michelle Robertson, Marianne Karplus, Lesley Parker, Kurt Feigl, John Akerley, Joe Greer, Janice Lopeman, Herb Wang, Elizabeth Berg, Dante Fratta, Craig Stenzel, Corné Kreemer, Cliff Thurber, Chelsea Lancelle, Cecil Hoffpauir, Bret Pecoraro, Bill Foxall, Ben Duggan, Athena Chalari, Andy Valentine, Amanda Thomas, and Alex Jensen. We also thank Jeff Wagoner, Drew Siler, Nicholas Hinz, and James Faulds for assistance with their geologic models.

Raw Synthetic Aperture Radar (SAR) data from the ERS, and Envisat satellite missions operated by the European Space Agency (ESA) are copyrighted by ESA and were provided through the WInSAR consortium at the UNAVCO facility. SAR data from the ALOS satellite mission operated by the Japanese Space Agency (JAXA) were acquired from NASA's Distributed Active Archive Center at the Alaska Satellite Facility (ASF). SAR data from the TerraSAR-X and TanDEM-X satellite missions operated by the German Space Agency (DLR) were acquired through Research Project RES1236.

Elena C. Reinisch was supported by the National Science Foundation Graduate Research Fellowship under grant DGE-1256259. The work presented herein was funded in part by the Office of Energy Efficiency and Renewable Energy (EERE), U.S. Department of Energy, under Award Numbers DE-EE0006760 and DE-EE0005510.

REFERENCES

Akerley, J. (2016), PoroTomo Subtask 6.8 - Brady Well Pumping Data During Deployment. http://dx.doi.org/0.15121/1334283

Ali, S. T., J. Akerley, E. C. Baluyut, M. Cardiff, N. C. Davatzes, K. L. Feigl, W. Foxall, D. Fratta, R. J. Mellors, P. Spielman, H. F. Wang, and E. Zemach (2016), Time-series analysis of surface deformation at Brady Hot Springs geothermal field (Nevada) using interferometric synthetic aperture radar, *Geothermics, 61*, 114-120. http://dx.doi.org/10.1016/j.geothermics.2016.01.008

Bakku, S. K. (2015), Fracture characterization from seismic measurements in a borehole, Ph.D. thesis, 227 pp, Massachusetts Institute of Technology.

Barry, K., D. Cavers, and C. Kneale (1975), Recommended standards for digital tape formats, *Geophysics, 40*, 344-352. http://library.seg.org/doi/abs/10.1190/1.1440530

Blewitt, G., C. Kreemer, W. C. Hammond, and J. Goldfarb (2013), Terrestrial reference frame NA12 for crustal deformation studies in North America, *Journal of Geodynamics, 72*, 11-24. http://dx.doi.org/10.1016/j.jog.2013.08.004

Coleman, T. (2013), A novel technique for depth discrete flow characterization: fibre optic distributed temperature sensing within boreholes sealed with flexible underground liners, MASc. thesis, University of Guelph.

Coolbaugh, M. F., C. Sladek, C. Kratt, and G. Edmondo (2004), Digital mapping of structurally controlled geothermal features with GPS units and pocket computers, *Geothermal Resources Council Transactions, 28*, 321-325.

Daley, T. M., D. E. Miller, K. Dodds, P. Cook, and B. M. Freifeld (2015), Field testing of modular borehole monitoring with simultaneous distributed acoustic sensing and geophone vertical seismic profiles at Citronelle, Alabama, *Geophysical Prospecting*. http://dx.doi.org/10.1111/1365-2478.12324

Doherty, J. (2001), PEST-ASP user's manual, *Watermark Numerical Computing, Brisbane, Australia*.

FairfieldNodal (2015), Typical specifications for FairfieldNodal ZLAND 3C seismometers, http://static.fairfieldnodal.com/assets/media/pdf/ZLand-3C-typical-specs.pdf

Faulds, J., I. Moeck, P. Drakos, and E. Zemach (2004), Structural assessment and 3D geological modeling of the Brady's geothermal area, Churchill county (Nevada, USA): A preliminary report, paper presented at Thirty-Fifth Workshop on Geothermal Reservoir Engineering, Stanford University, Stanford, California.

Faulds, J. E., and L. J. Garside (2003), Preliminary Geologic Map Of The Desert Peak - Brady Geothermal Fields, Churchill County, Nevada.

Faulds, J. E., M. F. Coolbaugh, G. S. Vice, and M. L. Edwards (2006), Characterizing Structural Controls of Geothermal Fields in the Northwestern Great Basin: A Progress Report, *Geothermal Resources Council Transactions, 30*, 69-76.

Faulds, J. E., M. F. Coolbaugh, D. Benoit, G. Oppliger, M. Perkins, I. Moeck, and P. Drakos (2010), Structural Controls of Geothermal Activity in the Northern Hot Springs Mountains, Western Nevada: The Tale of Three Geothermal Systems (Brady's, Desert Peak, and Desert Queen), *Geothermal Resources Council Transactions, 34*, 675-683.

Faulds, J. E., N. H. Hinz, M. F. Coolbaugh, P. H. Cashman, C. Kratt, G. Dering, J. Edwards, B. Mayhew, and H. Mclachlan (2011), Assessment of favorable structural settings of geothermal systems in the great basin region, western USA, paper presented at 2011 GSA Annual Meeting in Minneapolis.

Feigl, K. L., and PoroTomo_Team (2017), Overview and Preliminary Results from the PoroTomo Project at Brady Hot Springs, Nevada: Poroelastic Tomography by Adjoint Inverse Modeling of Data from Seismology, Geodesy, and Hydrology, paper presented at Stanford Geothermal Workshop, Stanford University. https://pangea.stanford.edu/ERE/db/GeoConf/papers/SGW/2017/Feigl.pdf

Harbaugh, A. W. (2005), *MODFLOW-2005, the US Geological Survey modular ground-water model: the ground-water flow process*, US Department of the Interior, US Geological Survey Reston.

Jolie, E., J. Faulds, and I. Moeck (2012), The development of a 3D structural-geological model as part of the geothermal exploration strategy - a case study from the Brady's geothermal system, Nevada, USA. , paper presented at 37th Workshop on Geothermal Reservoir Engineering, Stanford, California.

Jolie, E., I. Moeck, and J. E. Faulds (2015), Quantitative structural–geological exploration of fault-controlled geothermal systems—A case study from the Basin-and-Range Province, Nevada (USA), *Geothermics, 54*, 54-67. http://dx.doi.org/10.1016/j.geothermics.2014.10.003

Lancelle, C. (2016), Distributed Acoustic Sensing for Imaging Near-Surface Geology and Monitoring Traffic at Garner Valley, California, Ph.D. thesis thesis, University of Wisconsin-Madison.

Lim, D. D. (2016), PoroTomo Subtask 6.8 - Brady Well Coordinates and Observation Sensor Depths. http://dx.doi.org/10.15121/1261986

Lim, D. D. (2017), PoroTomo: Analysis of Pressure Data [data set]. https://gdr.openei.org/submissions/917

Lin, F.-C., D. Li, R. W. Clayton, and D. Hollis (2013), High-resolution 3D shallow crustal structure in Long Beach, California: Application of ambient noise tomography on a dense seismic array, *GEOPHYSICS, 78*, Q45-Q56. http://library.seg.org/doi/abs/10.1190/geo2012-0453.1

Lord, N., H. Wang, and D. Fratta (2016), A source-synchronous filter for uncorrelated receiver traces from a swept-frequency seismic source, *Geophysics, 81*, P47-P55. http://dx.doi.org/10.1190/geo2015-0324.1

Matzel, E., X. Zeng, C. Thurber, Y. Luo, C. Morency, and PoroTomo_Team (2017a), Seismic Interferometry Using the Dense Array at the Brady Geothermal Field (abstract SGP-TR-212), paper presented at Stanford Geothermal Workshop, Stanford University. https://pangea.stanford.edu/ERE/db/GeoConf/papers/SGW/2017/Matzel.pdf

Matzel, E., X. Zeng, C. Thurber, C. Morency, K. Feigl, and PoroTomo_Team (2017b), Using Virtual Earthquakes to Characterize the Material Properties of the Brady Hot Springs, Nevada paper presented at Geothermal Research Council Transactions, Salt Lake City. https://www.osti.gov/scitech/servlets/purl/1399706

Matzel, E., C. Morency, and D. Templeton (2018), Measuring the Material Properties Beneath Geothermal Fields Using Interferometry, paper presented at Stanford Geothermal Workshop.

Miller, D., T. Coleman, and PoroTomo_Team (2018), DAS and DTS at Brady Hot Springs: Observations about Coupling and Coupled Interpretations., paper presented at PROCEEDINGS, 43rd Workshop on Geothermal Reservoir Engineering, Stanford University, Stanford, California, February 12-14, 2018.

Parker, L. (2017), Active Source 3D Seismic Tomography of Brady Hot Springs Geothermal Field, Nevada, M.S. thesis, University of Wisconsin-Madison.

Parker, T., S. Shatalin, and M. Farhadiroushan (2014), Distributed Acoustic Sensing-A New Tool for Seismic Applications, *First Break, 32*, 61 - 69 http://fb.eage.org/publication/content?id=73487

Patterson, J., M. A. Cardiff, D. Lim, T. Coleman, H. F. Wang, K. L. Feigl, and PoroTomo_Team (2017a of Conference), H43E-1688: Characterization of Hydrologic and Thermal Properties at Brady Geothermal Field, NV. Thursday, 14 December 2017, 13:40 - 18:00, New Orleans Ernest N. Morial Convention Center - Poster Hall D-F abstract presented at Fall Meeting American Geophysical Union, New Orleans. https://agu.confex.com/agu/fm17/meetingapp.cgi/Paper/232589

Patterson, J. R., M. Cardiff, T. Coleman, H. Wang, K. L. Feigl, J. Akerley, and P. Spielman (2017b), Geothermal reservoir characterization using distributed temperature sensing at Brady Geothermal Field, Nevada, *The Leading Edge, 36*, 1024a1021 - 1024a1027. http://dx.doi.org/10.1190/tle36121024a1.1

Patterson, J. R., M. Cardiff, and K. L. Feigl (2018), Geothermal Reservoir Characterization Using Distributed Temperature Sensing at Brady Geothermal Field, Nevada, paper presented at PROCEEDINGS, 43rd Workshop on Geothermal Reservoir Engineering, Stanford University, Stanford, California,, February 12-14, 2018.

Reinisch, E. C., K. L. Feigl, M. A. Cardiff, C. Morency, C. Kreemer, J. Akerley, and PoroTomo_Team (2017 of Conference), Characterizing Volumetric Strain at Brady Hot Springs, Nevada, USA Using Geodetic Data, Numerical Models, and Prior Information, abstract presented at Fall Meeting American Geophysical Union, New Orleans. https://agu.confex.com/agu/fm17/meetingapp.cgi/Paper/233618

Reinisch, E. C., K. L. Feigl, and M. A. Cardiff (in prep), Characterizing Volumetric Strain at Brady Hot Springs, Nevada, USA Using Geodetic Data, Numerical Models, and Prior Information.

Shevenell, L., G. Oppliger, M. Coolbaugh, and J. Faulds (2012), Bradys (Nevada) InSAR Anomaly Evaluated With Historical Well Temperature and Pressure Data, *Geothermal Resources Council Transactions, 36*, 1383-1390.

Siler, D. L., J. E. Faulds, B. Mayhew, and D. D. McNamara (2016), Analysis of the favorability for geothermal fluid flow in 3D: astor Pass geothermal prospect, Great Basin, northwestern Nevada, USA, *Geothermics, 60*. http://dx.doi.org/10.1016/j.geothermics.2015.11.002

Thurber, C., X. Zeng, L. Parker, N. Lord, D. Fratta, H. Wang, E. M. Matzel, M. Robertson, K. L. Feigl, and PoroTomo_Team (2017 of Conference), Active-Source Seismic Tomography at Bradys Geothermal Field, Nevada, with Dense Nodal and Fiber-Optic Seismic Arrays, abstract presented at Fall Meeting American Geophysical Union, New Orleans. https://agu.confex.com/agu/fm17/meetingapp.cgi/Paper/213564

Wang, H., X. Zeng, D. Miller, D. Fratta, K. L. Feigl, and C. Thurber (submitted 2017/10/03), Ground Motion Response to a ML 4.3 Earthquake Using Co- Located Distributed Acoustic Sensing and Seismometer Arrays, *Geophys J Int*.

Wang, H. F., D. Fratta, N. Lord, C. Lancelle, K. Feigl, C. Thurber, X. Zeng, L. Parker, A. Chalari, D. Miller, and PoroTomo (2016 of Conference), Ground Motion Analysis of Co-Located DAS and Seismometer Sensors (abstract #S11D-2480) abstract presented at Fall Meeting Amer. Geophys. Un., San Francisco. https://agu.confex.com/agu/fm16/meetingapp.cgi/Paper/127717

Witter, J. B., D. L. Siler, J. E. Faulds, and N. H. Hinz (2016), 3D geophysical inversion modeling of gravity data to test the 3D geologic model of the Bradys geothermal area, Nevada, USA, *Geotherm Energy, 4*, 14. http://dx.doi.org/10.1186/s40517-016-0056-6

Zeng, X., C. Lancelle, C. Thurber, D. Fratta, H. Wang, A. Chalari, and A. Clarke (2017a), Properties of Noise Cross Correlation Functions Obtained from a Distributed Acoustic Sensing (DAS) Array at Garner Valley, California, *Bull. Seismol. Soc. Am., 107*. http://dx.doi.org/10.1785/0120160168

Zeng, X., C. H. Thurber, H. F. Wang, D. Fratta, and Porotomo_Team (2017b of Conference), 3D shear wave velocity structure revealed with ambient noise tomography on a DAS array (abstract #S33F-06), abstract presented at Fall Meeting Amer. Geophys. Un., New Orleans. https://agu.confex.com/agu/fm17/meetingapp.cgi/Paper/234986